Engineered Science
DOI: https://dx.doi.org/10.30919/es1401

On the Dynamic Instability of an Imperfect Microbeam under Magnetic and Thermal Excitations

Qais Atheabh, Ahmad Al-Qaisia and Ali H. Alhadidi*

Abstract

Magnetoelastic microbeams play a major role in various remote sensing and biomechanical applications. However, electromagnetic and thermal interactions are considered key challenges in magneto-solids mechanics. To this end, this research paper investigates the regions of dynamic instability and the transient response of a microbeam subjected to periodic transverse magnetic fields and thermal loads. The study employs a magnetoelastic model of a micro-beam with an imperfection represented by a half-sine rise. The material is characterized as nonlinear thermoelastic, incorporating nonlinear strain. The governing partial differential equation of motion is obtained as a nonlinear, time-dependent Mathieu's equation, employing Galerkin's method and considering the first mode shape. The investigation of dynamic instability is conducted utilizing the incremental harmonic balance method. The effect of the variations in the initial rise, temperature increment, and amplitude on the dynamic instability are illustrated and analyzed. In addition, the transient midspan vibration is studied under various cases involving alterations in transverse magnetic field strength, temperature increment, and oscillating transverse magnetic field excitation frequency, with and without initial rise. Finally, deliberate variations in the excitation frequency are selected to examine the system dynamic transitions across the instability boundary, revealing the presence of beating and pseudo-unstable phenomena.

Keywords: Dynamic instability; Nonlinear dynamics; Microbeams; Initial rise.
Received: 18 November 2024; Revised: 31 December 2024; Accepted: 12 January 2025.
Article type: Research article.

1. Introduction

Mechanical microbeams are the cornerstones of Micro-Electro-Mechanical Systems (MEMS),[1] which are utilized in diverse applications in various engineering fields such as aerospace engineering,[2] automotive engineering,[3] energy harvesting,[4] and biomedical engineering.[5] Since microbeams offer many significant advantages, such as high sensitivity, low power consumption, and fast time response, they are essential components in the development of cutting-edge technologies and innovations. Pre-shaped (initially risen) microbeams provide further unique advantages, including reduced deflection and tunable fundamental frequency and mode shapes.[6] In light of the interactions between magnetoelastic solids and magnetic fields on a micro-level, remarkable developments have been achieved in terms of remote sensing,[7] remote actuating systems,[8] and micro-biomedical applications.

Department of Mechanical Engineering, University of Jordan, Amman 11942, Jordan
orcid.org/0000-0003-3995-3629; **Email:* ahadidi@ju.edu.jo (A. Alhadidi)

The ambiguous treatment of the interactions of electromagnetic fields with deformable structures was one of the involved problems of magneto-solids mechanics since magneto-solids mechanics emerges from the nonlinear interactions between the structures' nonlinear magnetization and the applied magnetic field. These phenomena attracted many researchers' attention due to their practical significance. Moon and Pao proposed the first mathematical model incorporating distributed magnetic loadings and experimentally discovered the magnetoelastic buckling and the parametric instability of a cantilever beam-plate in a uniform transverse magnetic field.[9,10] Subsequently, many researchers focused on elucidating these results. Where experimental and theoretical results are deviated by a factor of two. Dalrymple et *al*.[11] conducted an experimental investigation that suggested specific criteria must be satisfied in an experimental program, and the finite size of a specimen must be assumed in theoretical treatments. Miya *et al*.[12] applied a finite element investigation and assumed that the magnetic torque is proportional to the rotation of the plate. Christopherson *et al*.[13] studied the magnetoelastic buckling by calculating the bending moment diagram of the specimen

using the strain and field measurements. The findings were also compared with the Moon-Pao model.[9] The dynamic instability of a magnetoelastic beam in a periodic transverse magnetic field has become a subject of interest for many researchers. Shih *et al*.[14] and Wu *et al*.[15] investigated the dynamic stability of an elastic beam subjected to pulsating axial load and oscillating transverse magnetic field under different loading conditions. Wu (2005) studied the dynamic instability and transient vibrations of a pinned beam subjected to both a transverse magnetic field and thermal load for small vibration amplitudes. The study took into consideration the influence of temperature variations on conductivity.[16] Similarly, another study has been conducted for large amplitudes with nonlinear strain and nonlinear thermoelastic material by Wu (2007).[17] Lu *et al*.[18] developed a mathematical model of a magnetoelastic buckled beam immersed in a periodic transversal magnetic field and exposed to an external axial periodic force.

Recently, microbeams have been studied in longitudinal magnetic fields.[19-21] Wang *et al*.[19] investigated the dynamic instability of a current-carrying microbeam in a longitudinal magnetic field model. The study illustrated that increasing the magnetic field parameter is associated with natural frequency reduction. Additionally, functionally graded microbeams, being immersed in a magnetic field, have been investigated.[22,23] Due to the importance of pre-shaped microbeams,[24] recent studies have been focused on investigating curved microbeams under magnetic and thermal loads.[25,26] Allahkarami *et al*.[25] examined the dynamic stability of an embedded curved microbeam reinforced by functionally graded carbon nanotubes that are subjected to magnetic, thermal, and harmonic mechanical loads using the differential quadrature method. The study's outcomes show that increasing the magnetic field intensity and reducing the central angle of the curved microbeam leads to a shift of the dynamic stability region towards higher frequencies. On the other hand, as the temperature increases, the instability region shifts towards lower frequencies.

To our knowledge, all previous studies related to magnetoelastic pre-shaped, *i.e.*, imperfect microbeams with initial rise, have assumed the magnetic fields to be constant. This article presents an investigation of the dynamic instability of a magnetoelastic microbeam with an initial rise under periodic transverse magnetic field excitation and thermal loading. The proposed model, a magnetoelastic microbeam with an initial rise under periodic transverse magnetic field excitation and thermal load, can be utilized in remote actuation systems, such as bio-mechanical applications where spaces are limited and power integration is challenging. In addition, this study has considered the presence of an initial rise, which may arise from fabrication-induced residual stress. Alternatively, it can be intentionally introduced, in combination with thermal loading, to tune the fundamental natural frequencies. The main objectives of this study are the dynamic instability and transient vibrations of a pinned magnetoelastic microbeam with an initial imperfection. The beam is considered to exhibit a nonlinear thermoelastic material property and with nonlinear stain. The microsystem is subjected to oscillating transverse magnetic field excitation and thermal load. The governing equation of the proposed model is derived using Hamilton's principle. Applying Galerkin's method, the equation of motion is discretized into a strong nonlinear time-dependent Mathieu equation, which represents the midspan deflection. The midspan transient vibration is obtained using numerical simulations. The dynamic instability region is determined by exploiting the incremental harmonic balance (IHB) method.[17,27] The principal instability regions are shown in the parameter space of the excitation magnitude versus frequency ratio. Finally, the steady-state solution is obtained using the method of multiple scales (MMS), and the results are numerically validated.

2. Mathematical model

In this study, the proposed model is a magnetoelastic pinned microbeam of width d, thickness h, and length L, pre-shaped by half sine rise $v_0(x) = V_0 \sin\left(\frac{\pi}{L}x\right)$ represents the initial rise value, as shown in Fig. 1 The beam is subjected to a periodic uniform transverse magnetic field $B_0(t) = B_m \cos(\varpi t)\vec{j}$ and a uniform temperature increment ΔT. The generated magnetic force results in a displacement (u, v) of the microbeam, with u representing the longitudinal displacement and v representing the transverse displacement. The microbeam exhibits material properties that are both homogenous and isotropic. The thickness, initial rise, and deflection of the microbeam are presumed to be considerably smaller than its length.

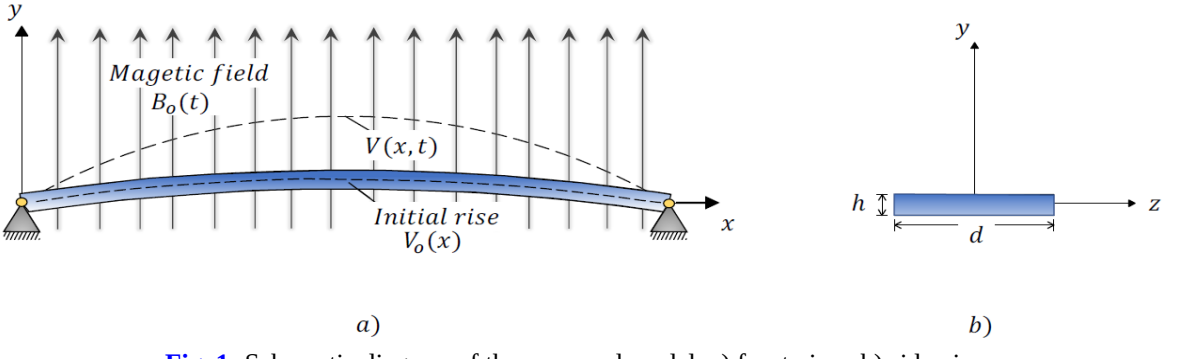

Fig. 1: Schematic diagram of the proposed model: a) front view, b) side view.

2.1 Hamilton's principle

The derivation of the mathematical model for the elastic system involves expressing the integral of the Lagrangian function, denoted as I_L, in the following Eq. (1):

$$I_L = \int_{t_1}^{t_2}(K + W - U)dt \tag{1}$$

where K represents the kinetic energy of the system, W denotes the work done by non-conservative forces, and U stands for the potential energy. The variation in I_L results in Eq. (2):

$$\delta I_L = \int_{t_1}^{t_2}\delta(K + W - U)dt = 0 \tag{2}$$

In the present study, the nonlinear strain due to material properties and the initial rise takes the following form Eq. (3):

$$\varepsilon_{xx} = \frac{\partial u}{\partial x} + \frac{1}{2}\left(\frac{\partial v}{\partial x}\right)^2 + \frac{\partial v}{\partial x}\frac{\partial v_0}{\partial x} \tag{3}$$

The elastic strain energy arising from nonlinear strain and a temperature increment (ΔT) can be formulated using Eq. (4):

$$U = \frac{EI}{2}\int_0^L\left(\frac{\partial^2 v}{\partial x^2}\right)^2 dx + \frac{A}{2E}\int_0^L\left[E\left(\frac{\partial u}{\partial x} + \frac{1}{2}\left(\frac{\partial v}{\partial x}\right)^2 + \frac{\partial v}{\partial x}\frac{\partial v_0}{\partial x}\right) - \gamma(\Delta T)\right]^2 dx \tag{4}$$

where I is the second moment of mass, E is the modulus of elasticity, A is the cross-sectional area, and $\gamma(\Delta T)$ is the stress temperature coefficient, which is considered in the form Eq. (5).[28]

$$\gamma(\Delta T) = E\alpha\Delta T + \bar{h}\,\alpha^2\Delta T^2 \tag{5}$$

where α is the thermal expansion coefficient, and

$$\bar{h} = \bar{h}_1(1 - 2\nu) - 2\bar{h}_2(\nu^2 - 1) + \bar{h}_3\nu^2 \tag{6}$$

In Eq. (6), $\bar{h}_1$, $\bar{h}_2$, and $\bar{h}_3$ are Murnaghan's constants. Kinetic energy and the work of externally applied force are expressed as the following Eqs. (7) and (8), respectively.

$$K = \frac{1}{2}\int_0^L m\left(\frac{\partial v}{\partial t}\right)^2 dx \tag{7}$$

$$W_P = \int_0^L N(ds - dx) = \frac{1}{2}\int_0^L\left(\int_0^x p\,d\xi\right)\left(\frac{\partial v}{\partial x}\right)^2 dx \tag{8}$$

In this context, m represents the mass distributed per unit length of the microbeam, N stands for the axial compressive force applied to the microbeam, and p denotes the body force per unit length.

Variations in kinetic energy, work done by externally applied forces and couple, and potential energy. Respectively. Therefore, estimating energy variations, Eq. (2) can be expanded as Eq. (9):

$$\delta I_L = \int_{t_1}^{t_2}\int_0^L q_1\,dxdt + \int_{t_1}^{t_2} q_2\,dt + \int_{t_1}^{t_2} q_3\,dt - \int_{t_1}^{t_2}\int_0^L q_4\,dx\,dt - \int_{t_1}^{t_2}\int_0^L q_5\,dxdt = 0\int_{t_1}^{t_2}\int_0^L q_5\,dxdt = 0 \tag{9}$$

where terms q_1 to q_5 are defined as Eqs. (10)-(14):

$$q_1 = m\left(\frac{\partial^2 v}{\partial t^2}\right)\delta v + \frac{\partial c}{\partial x}\delta v + \frac{\partial}{\partial x}\left[\left(\int_0^x p\,d\xi\right)\left(\frac{\partial v}{\partial x}\right)\right]\delta v + EI\frac{\partial^4 v}{\partial x^4}\delta v - EA\frac{\partial}{\partial x}\left[\left(\frac{1}{2}\left(\frac{\partial v}{\partial x}\right)^2 + \frac{\partial v}{\partial x}\frac{\partial v_0}{\partial x}\right)\left(\frac{\partial v}{\partial x} + \frac{\partial v_0}{\partial x}\right)\right]\delta v - EA\frac{\partial}{\partial x}\left[\left(\frac{\partial u}{\partial x} - \frac{\gamma(\Delta T)}{E}\right)\left(\frac{\partial v}{\partial x} + \frac{\partial v_0}{\partial x}\right)\right]\delta v \tag{10}$$

$$q_2 = \left\{\begin{array}{c} -m\left(\frac{\partial v}{\partial t}\right)\delta v - c\delta v - \left(\int_0^x p\,d\xi\right)\left(\frac{\partial v}{\partial x}\right)\delta v \\ +EI\frac{\partial^2 v}{\partial x^2}\frac{\partial}{\partial x}(\delta v) - EI\frac{\partial^3 v}{\partial x^3}\delta v + \\ EA\left(\frac{\partial u}{\partial x} + \frac{1}{2}\left(\frac{\partial v}{\partial x}\right)^2 + \frac{\partial v}{\partial x}\frac{\partial v_0}{\partial x} - \frac{\gamma(\Delta T)}{E}\right)\left(\frac{\partial v}{\partial x} + \frac{\partial v_0}{\partial x}\right)\delta v \end{array}\right\}\Bigg|_0^L \tag{11}$$

$$q_3 = EA\frac{\partial}{\partial x}\left[\frac{\partial u}{\partial x} + \frac{1}{2}\left(\frac{\partial v}{\partial x}\right)^2 + \frac{\partial v}{\partial x}\frac{\partial v_0}{\partial x} - \frac{\gamma(\Delta T)}{E}\right]\delta u\Big|_0^L \tag{12}$$

$$q_4 = EA\frac{\partial}{\partial x}\left[\frac{1}{2}\left(\frac{\partial v}{\partial x}\right)^2 + \frac{\partial v}{\partial x}\frac{\partial v_0}{\partial x}\right]\delta u \tag{13}$$

$$q_5 = EA\frac{\partial}{\partial x}\left[\frac{\partial u}{\partial x} - \frac{\gamma(\Delta T)}{E}\right]\delta u \tag{14}$$

Given the beam model is supported with pinned ends at $x = 0$ and L, the boundary conditions can be established as follows Eqs. (15) and (16):

$$u(0) = \delta u(L) = \delta v(0) = \delta v(L) = 0 \tag{15}$$

$$v(0) = v(L) = 0 \quad and \quad v''(0) = v''(L) = 0 \tag{16}$$

The equations describing the motion equilibrium, in addition to the defined boundary conditions, can be derived in the following manner:

$$EA\frac{\partial}{\partial x}\left[\frac{\partial u}{\partial x} - \frac{\gamma(\Delta T)}{E}\right] = 0 \tag{17}$$

$$EA\frac{\partial}{\partial x}\left[\frac{1}{2}\left(\frac{\partial v}{\partial x}\right)^2 + \frac{\partial v}{\partial x}\frac{\partial v_0}{\partial x}\right] = 0 \tag{18}$$

$$m\left(\frac{\partial^2 v}{\partial t^2}\right) + EI\frac{\partial^4 v}{\partial x^4} + \frac{\partial c}{\partial x} + \frac{\partial}{\partial x}\left[\left(\int_0^x p\,d\xi\right)\left(\frac{\partial v}{\partial x}\right)\right] - EA\frac{\partial}{\partial x}\left[\left(\frac{1}{2}\left(\frac{\partial v}{\partial x}\right)^2 + \frac{\partial v}{\partial x}\frac{\partial v_0}{\partial x}\right)\left(\frac{\partial v}{\partial x} + \frac{\partial v_0}{\partial x}\right)\right] - EA\frac{\partial}{\partial x}\left[\left(\frac{\partial u}{\partial x} - \frac{\gamma(\Delta T)}{E}\right)\left(\frac{\partial v}{\partial x} + \frac{\partial v_0}{\partial x}\right)\right] = 0 \tag{19}$$

It is evident from Eq. (17) that,

$$\frac{\partial u}{\partial x} - \frac{\gamma(\Delta T)}{E} = constant = \overline{\delta}(\Delta T) \tag{20}$$

Consequently, $\overline{\delta}(\Delta T)$ in Eq. (20) can be defined as:

$$\overline{\delta}(\Delta T) = \frac{1}{L}\int_0^L\left[\frac{\partial u}{\partial x} - \frac{\gamma(\Delta T)}{E}\right]dx = \frac{-\gamma(\Delta T)}{E} \tag{21}$$

Similarly, a deduction can be drawn from Eq. (18) as follows:

$$\frac{1}{2}\left(\frac{\partial v}{\partial x}\right)^2 + \frac{\partial v}{\partial x}\frac{\partial v_0}{\partial x} = \frac{1}{L}\int_0^L\left[\frac{1}{2}\left(\frac{\partial v}{\partial x}\right)^2 + \frac{\partial v}{\partial x}\frac{\partial v_0}{\partial x}\right]dx = constant \tag{22}$$

By substituting Eqs. (21) and (22) into Eq. (19), the equation of motion can be expressed as Eq. (23):

$$m\frac{\partial^2 v}{\partial t^2} + EI\frac{\partial^4 v}{\partial x^4} + \frac{\partial c}{\partial x} + \frac{\partial}{\partial x}\left[\left(\int_0^x p\,d\xi\right)\left(\frac{\partial v}{\partial x}\right)\right] - \frac{EA}{L}\int_0^L\left[\frac{1}{2}\left(\frac{\partial v}{\partial x}\right)^2 + \frac{\partial v}{\partial x}\frac{\partial v_0}{\partial x}\right]dx\left(\frac{\partial^2 v}{\partial x^2} + \frac{\partial^2 v_0}{\partial x^2}\right) + A\gamma(\Delta T)\left(\frac{\partial^2 v}{\partial x^2} + \frac{\partial^2 v_0}{\partial x^2}\right) = 0 \tag{23}$$

2.2 Electromagnetic force

A magnetoelastic volume V experiences the electromagnetic force $\mathbf{F}$ and torque $\mathbf{c}$, according to Ref. [16], which can be expressed as Eqs. (24) and (25):

$$\boldsymbol{F} = \int \sigma(\dot{\boldsymbol{r}} \times \mathbf{B}_0) \times \mathbf{B}_0 dV \tag{24}$$

$$\boldsymbol{c} = \int \mathbf{M} \times \mathbf{B}_0\, dV \tag{25}$$

where σ is the conductivity, $\dot{\boldsymbol{r}}$ is the velocity, $\mathbf{B}_0$ is the magnetic field, and $\mathbf{M} = \chi(\mu_0\mu_r)^{-1}\mathbf{B}$ is the density of magnetization within the body's volume. μ_0 is the permeability of the vacuum, μ_r is the relative permeability, $\chi = 1 - \mu_r$ is the susceptibility, and $\mathbf{B}$ is the magnetic induction vector, $\boldsymbol{c}$ stands for the body couple per unit length.

3. Analytical approach

3.1 Displacement and initial rise functions

Utilizing Galerkin's procedure using the single-mode approach in the present study, the displacement function is given by:

$$v(x,t) = w(t)\sin(\lambda x),\ 0 \le x \le L \tag{26}$$

The initial rise function can be written as:

$$v_0(x) = V_0 \sin(\lambda x), \quad 0 \le x \le L \tag{27}$$

where $\lambda = \frac{\pi}{L}$. A beam length s with initial rise, as derived in Ref. [29], is

$$s = \int_0^x \sqrt{1 + \left(v'(\xi, t) + v_0'(\xi, t)\right)^2}\, d\xi \tag{28}$$

Differentiating Eq. (28) with respect to time assuming an inextensible beam, rearranging, and substituting Eqs. (26) and (27), the velocity in the x direction can be expressed as:

$$\dot{x} = \frac{-1}{\left(1+(v'+v_0')^2\right)^{\frac{1}{2}}} \int_0^x \frac{(v'+v_0')(\dot{v}'+\dot{v}_0')}{\sqrt{1+(v'+v_0')^2}}\, d\xi \tag{29}$$

For small deflection and small initial rise compared to beam length $\sqrt{1 + (\lambda \cos(\lambda x))^2 (w + V_0)^2} \cong 1$, Eq. (29) becomes:

$$\dot{\boldsymbol{r}}(x, w) = \dot{x} = -\int_0^x (\lambda \cos(\lambda x))^2 \dot{w}(w + V_0)\, d\xi = -\lambda^2 (w + V_0)\dot{w} \left(\frac{\sin(2\lambda x)}{4\lambda} + \frac{x}{2}\right) \tag{30}$$

Substituting it in Eq. (24), electromagnetic force can be rewritten as:

$$\boldsymbol{F} = p\vec{\imath} = -\left(\frac{\sigma}{2}\right) h d B_m^2 (1 + \cos(2\varpi t))\dot{\boldsymbol{r}}(x, w)\vec{\imath} \tag{31}$$

The magnetization **M** can be determined as described in Ref. [9], and body couple can be acquired as:

$$\boldsymbol{c} = \int M \times B_0 dV = \lambda \Phi d \cos(\lambda x)(1 + \cos(2\varpi t))w\vec{k} \tag{32}$$

where $\Phi = \frac{\chi^2 B_m^2 \sinh(\lambda h/2)}{\mu_0 \mu_r \lambda \Delta}$, $\Delta = \mu_r \sinh\left(\frac{\lambda h}{2}\right) + \cosh\left(\frac{\lambda h}{2}\right)$.

Substituting Eqs. (30)-(32) into Eq. (23) leads to a linear operator $\Pi(w)$ using Eq. (33).

$$\Pi(w) = \left\{ m\ddot{w} + EI\lambda^4 w - \lambda^2 \Phi (1 + cos(2\varpi t))w + \frac{EA}{2}\lambda^4 \left[\frac{1}{2}w^3 + \frac{3}{2}V_0 w^2 + {V_0}^2 w\right] - A\gamma(\Delta T)(w + V_0)\lambda^2 \right\} \sin(\lambda x) - \frac{\sigma}{2} h d B_m^2 (1 + cos(2\varpi t))\left[\lambda w cos(\lambda x)\dot{r}(x, w) - \lambda^2 w \sin(\lambda x) \int_0^x \dot{\boldsymbol{r}}(x, w) dx\right] = 0 \tag{33}$$

3.2 Temperature effects

A material resistivity ϑ varies with temperature and is governed by Eq. (34). Furthermore, the conductivity (σ) and resistivity of a material are inversely associated, $\sigma = 1/\vartheta$.

$$\vartheta = \vartheta_0 + \vartheta_0 \alpha_r \Delta T \tag{34}$$

where ϑ_0 is the resistivity at room temperature, and α_r is the temperature coefficient of resistivity. The restraining force imposed by the boundaries cancels out the thermal expansion. When the nonlinear stress-temperature coefficient $\gamma(\Delta T)$ is identified, the restraining force P_t can be expressed as follows Eq. (35).

$$P_t = -EA\alpha\Delta T - hA\alpha^2 \Delta T^2 \tag{35}$$

3.3 Galerkin's method

Taking $\sin(\lambda x)$ as the fundamental function, the Galerkin equation yields in Eq. (36).

$$\int_0^L \Pi(w) \sin(\lambda x)\, dx = 0 \tag{36}$$

A time-dependent nonlinear Matheu differential equation is obtained as:

$$\frac{d^2 w}{dt^2} + 2\xi(1 + cos(2\varpi t))(w^2 + V_0 w)\frac{dw}{dt} + (\omega_L^2 - \psi \cos(2\varpi t))w + \varsigma w^2 + \eta w^3 - K = 0 \tag{37}$$

where $2\xi = \left(\frac{-18-8\pi^2}{192}\right)\frac{\sigma B_m^2 \lambda^2}{\rho}$, $\omega_0^2 = \frac{E\lambda^4(2I+AV_0^2)}{2\rho h d}$, $\omega_L^2 = \omega_0^2\left(1 - \frac{2(EA\alpha\Delta T + \bar{h}A\alpha^2\Delta T^2)}{E\lambda^2(2I+AV_0^2)} - \frac{B_r^2}{B_c^2}\right)$, $\psi = \frac{\lambda^2 \Phi}{\rho h}$, $\varsigma = \frac{3}{4}\frac{E\lambda^4 V_0}{\rho}$, $\eta = \frac{1}{4}\frac{E\lambda^4}{\rho}$, $B_c^2 = \frac{E\lambda^3(2I+AV_0^2)\mu_0\mu_r\Delta}{4\chi^2 d \sinh(\lambda h/2)}$, $B_r^2 = \frac{B_m^2}{2}$, $K = \frac{(E\alpha\Delta T + \bar{h}\alpha^2\Delta T^2)V_0\lambda^2}{\rho}$, ρ is the density of the microbeam, B_c is the first mode buckling field of the system, ω_0 is the natural frequency, and ω_L is the fundamental natural frequency. For instability analysis, it is customary to introduce new variables: the reduced natural frequency $\Omega = \varpi/\omega_L$, a new time scale $\tau = \varpi t$, $\varphi = B_r^2/B_c^2$. Introducing the new variables to Eq. (37) leads to:

$$\Omega^2 \frac{d^2 w}{d\tau^2} + O\varphi\Omega(1 + cos(2\tau))(w^2 + V_0 w)\frac{dw}{d\tau} + \left(1 - \theta - \varphi(1 + \cos(2\tau))\right)w + \mu w^2 + \beta w^3 - k = 0 \tag{38}$$

where $O = \frac{(-18-8\pi^2)\sigma\lambda^2 B_c^2}{96\rho\omega_0}$, $\theta = \frac{2(EA\alpha\Delta T + \bar{h}A\alpha^2\Delta T^2)}{E\lambda^2(2I+AV_0^2)}$, $\mu = \frac{3}{4}\frac{E\lambda^4 V_0}{\rho\omega_0^2}$, $\beta = \frac{1}{4}\frac{E\lambda^4}{\rho\omega_0^2}$, $k = \frac{(E\alpha\Delta T + \bar{h}\alpha^2\Delta T^2)V_0\lambda^2}{\rho\omega_0^2}$

3.4 IHB method

The procedure of solving Eq. (38) using the method consists of two steps, as outlined in the references.[27,30] In the first step, the Newton-Raphson method is employed to solve a system of linear equations. Once a periodic solution denoted as w_0, associated with a point (φ_0, Ω_0) located on the instability boundary, is identified, additional points along the instability boundary and their respective solutions can be obtained through incremental steps as follows Eq. (39):

$$\varphi = \varphi_0 + \Delta\varphi, \ \Omega = \Omega_0 + \Delta\Omega, \ w = w_0 + \Delta w \tag{39}$$

Inserting these expressions into Eq. (38) and retaining only the linear terms of increments $\Delta\varphi$, $\Delta\Omega$, Δw, a linearized incremental equation is obtained as follows in Eq. (40):

$$\Omega_0^2 \Delta\ddot{w} + 2\varphi_0\Omega_0 O\, cos(\tau)^2 (w_0^2 + V_0 w_0)\Delta\dot{w} + (1 - \theta + 3\beta w_0^2 - 2\varphi_0\, cos(\tau)^2 + 2\mu w_0 + 2\varphi_0\Omega_0 O\, cos(\tau)^2 (2w_0 + V_0)\dot{w}_0)\Delta w = R - \Delta\varphi(2\Omega_0 O\, cos(\tau)^2 (w_0^2 + V_0 w_0)\dot{w}_0 - 2\, cos(\tau)^2 w_0) - \Delta\Omega(2\Omega_0\ddot{w}_0 + 2\varphi_0 O\, cos(\tau)^2 (w_0^2 + V_0 w_0)\dot{w}_0) \tag{40}$$

where $R = -(\Omega_0^2\ddot{w}_0 + 2\varphi_0\Omega_0 O\, cos(\tau)^2 (w_0^2 + V_0 w_0)\dot{w}_0 + (1 - \theta - 2\varphi_0\, cos(\tau)^2)w_0 + \mu w_0^2 + \beta w_0^3 - k)$

In the second step, assuming an approximate periodic solution, Galerkin's Method is applied as Eqs. (41) and (42):

$$w_0(\tau) = \sum_{k=0}^N (a_k \sin k\tau + b_k \cos k\tau) \tag{41}$$

$$\Delta w(\tau) = \sum_{k=0}^N (\Delta a_k \sin k\tau + \Delta b_k \cos k\tau) \tag{42}$$

Referring to the primary region of instability associated with a solution of period 2π. N is the number of temporal terms. In this study, the first five harmonic terms are considered, and according to Ref. [27], the first three harmonic odd terms are adequate to give a high level of accuracy. By inserting Eq. (42) into Eq. (40) and employing the Galerkin's method, a system of linear equations can be obtained as follows:

$$[C]\{\Delta a\} = \{R\} + \Delta\varphi\{P\} + \Delta w\{Q\} \tag{43}$$

where $[C]$ is a matrix of Fourier coefficients, $\{\Delta a\}$ is a column vector comprising Fourier coefficients Δa_k or Δb_k. $\{R\}$ represents the corrective vector obtained from Eqs. (41) and (42), $\{P\}$, and $\{Q\}$ are vectors derived from the second and

third right-hand side terms, respectively.

Two constraints, $\Delta\varphi = 0.01$ and $\|a\| = \|a + \Delta a\|$ are introduced to Eq. (43) owing to its $2N + 2$ unknows. Both constraints remained unchanged throughout each increment. In this research, the Euclidian norm was employed as Eq. (44):

$$\|a\| = [\sum_{k=1}^{N}(a_k^2 + b_k^2)]^{1/2} \quad (44)$$

3.5 MMS

In this section, we utilize the MMS to investigate the steady state response of the structure.[31] Scaling parameter ϵ is applied to nonlinear terms in Eq. (37) as follows Eq. (45):

$$\frac{d^2w}{dt^2} + 2\xi\epsilon(1 + cos(2\varpi t))(w^2 + V_0 w)\frac{dw}{dt} + (\omega_L^2 - \psi\,\epsilon\cos(2\varpi t))w + \varsigma\epsilon w^2 + \eta\epsilon w^3 - \epsilon K = 0 \quad (45)$$

Expanding time dependence into ordinary and slow time scales in the following $T_1 = \epsilon t$, respectively. The time derivatives, considering both scales, can be formulated as Eq. (46):

$$\frac{d}{dt} = D_0 + \epsilon D_1 + O(\epsilon^2),\ \frac{d^2}{dt^2} = {D_0}^2 + 2\epsilon D_0 D_1 + O(\epsilon^2) \quad (46)$$

Midspan displacement function $w(t)$ can be expanded from Eq. (37) in the following Eq. (47):

$$w = w_1(T_0, T_1) + \epsilon w_2(T_0, T_1) + O(\epsilon^2) \quad (47)$$

Substituting both time scales and their derivatives into Eq. (45). Then, collecting terms of equal power of ϵ results in the following Eqs. (48) and (49):

$$O(\epsilon^0): {D_0}^2 w_1 + {\omega_L}^2 w_1 = 0 \quad (48)$$

$$O(\epsilon): {D_0}^2 w_2 + {\omega_L}^2 w_2 = 2\psi\cos^2(\varpi T_0)w_1 - 4\xi\cos^2(\varpi T_0)\,{w_1}^2 D_0 w_1 - 2D_0 D_1 w_1 - \varsigma {w_1}^2 - \eta {w_1}^3 - \psi w_1 - 4\xi\cos^2(\varpi T_1)V_0 w_1 D_1 w_1 + K \quad (49)$$

The general solution of Eq. (48) can be expressed in a complex form Eq. (50).

$$w_1 = A(T_1)e^{i\omega_L T_0} + \bar{A}(T_1)e^{-i\omega_L T_0} \quad (50)$$

Rewriting Eq. (49) in the complex form yields:

$$\begin{aligned}{D_0}^2 w_2 + {\omega_L}^2 w_2 = {} & (-2i\xi A^3\omega_L - A^3\eta)e^{3i\omega_L T_0} - iA^2\xi V_0\omega_L e^{2iT_0(\omega_L - \varpi)} - iA^2 V_0\xi\omega_L e^{2iT_0(\omega_L + \varpi)} + \\ & e^{iT_0(\omega_L + 2\varpi)}\left(\frac{1}{2}A\psi - iA^2\bar{A}\omega_L\xi\right) + e^{iT_0(\omega_L - 2\varpi)}\left(\frac{1}{2}A\psi - iA^2\bar{A}\omega_L\xi\right) + e^{2i\omega_L T_0}(-2iA^2 V_0\omega_L\xi - \varsigma A^2) + \\ & e^{iT_0(3\omega_L + 2\varpi)}(-i\xi A^3\omega_L) + e^{iT_0(3\omega_L - 2\varpi)}(-i\xi A^3\omega_L) + \\ & e^{i\omega_L T_0}\left(-3A^2\bar{A}\eta - 2i\omega_L\frac{dA}{dT_2} - 2iA^2\bar{A}\omega_L\xi\right) + CC + K - 2A\bar{A}\varsigma \end{aligned} \quad (51)$$

Eliminating secular terms in the right-hand side of Eq. (51) yields the following:

$$-3A^2\bar{A}\eta - 2i\omega_L\frac{dA}{dT_2} - 2iA^2\bar{A}\omega_L\xi = 0 \quad (52)$$

Assuming that A and $\bar{A}$ in the following complex form are given by $A(T_1) = \frac{1}{2}a(T_1)e^{ib(T_1)}$ and $\bar{A}(T_1) = \frac{1}{2}a(T_1)e^{ib(T_1)}$, substituting these terms into Eq. (52) and equating real terms and imaginary terms to zero leads to the following Eqs. (53) and (54), respectively.

$$\frac{3}{8}a^3\eta - \omega_L a\frac{db}{dT_2} = 0 \quad (53)$$

$$\omega_L\frac{da}{dT_1} + \frac{1}{4}a^3\omega_L\xi = 0 \quad (54)$$

Furthermore, w_1 can be rewritten in the following form Eq. (55):

$$w_1 = a\,cos(\omega_L T_1 + b) \quad (55)$$

Applying the boundary conditions $w(0,0) = w_i$, and $\dot{w}(0,0) = 0$, where w_i is the initial displacement, results in the following Eq. (56):

$$a(0) = w_i,\ \ b(0) = 0 \quad (56)$$

Solving Eqs. (53) and (54) with respect to the boundary conditions yield Eqs. (57) and (58), respectively.

$$a(T_1) = \frac{2w_i}{\sqrt{2T_1 {w_i}^2\xi + 4}} \quad (57)$$

$$b(T_1) = \frac{3}{4}\frac{\eta\ln(T_1 {w_i}^2\xi + 2)}{\omega_L\xi} - \frac{3}{4}\frac{\eta\ln(2)}{\omega_L\xi} \quad (58)$$

The particular solution of Eq. (51) can be expressed in the following Eq. (59):

$$\begin{aligned} w_2 = {} & A_1\sin(\omega_L T_0 + b + 2\varpi T_0) + A_2\sin(\omega_L T_0 + b - 2\varpi T_0) + A_3\sin(2\omega_L T_0 + 2b + 2\varpi T_0) + A_4\sin(2\omega_L T_0 + 2b - 2\varpi T_0) + A_5\sin(2\omega_L T_0 + 2b) + A_6\cos(2\omega_L T_0 + 2b) + A_7\sin(3\omega_L T_0 + 3b) + A_8\cos(3\omega_L T_0 + 3b) + \\ & A_9\cos(\omega_L T_0 + b - 2\varpi T_0) + A_{10}\cos(\omega_L T_0 + b + 2\varpi T_0) + A_{11}\sin(3\omega_L T_0 + 3b + 2\varpi T_0) + A_{12}\sin(3\omega_L T_0 + 3b - 2\varpi T_0) + A_{13} \end{aligned} \quad (59)$$

where

$$A_1 = -\frac{1}{16}\frac{\xi a^3\omega_L}{\varpi(\varpi + \omega_L)},\ \ A_2 = -\frac{1}{16}\frac{\xi a^3\omega_L}{\varpi(\varpi - \omega_L)},$$

$$A_3 = -\frac{1}{2}\frac{\xi V_0 a^2\omega_L}{(2\varpi + 3\omega_L)(2\varpi + \omega_L)},$$

$$A_4 = -\frac{1}{2}\frac{\xi V_0 a^2\omega_L}{(2\varpi - \omega_L)(2\varpi - 3\omega_L)},\ \ A_5 = -\frac{1}{3}\frac{\xi V_0 a^2}{\omega_L},$$

$$A_6 = \frac{1}{6}\frac{a^2\varsigma}{\omega_L},\ \ A_7 = -\frac{1}{16}\frac{a^3\xi}{\omega_L},\ A_8 = \frac{1}{32}\frac{a^3\eta}{\omega_L},$$

$$A_9 = -\frac{1}{8}\frac{a\psi}{\varpi(\varpi - \omega_L)},\ A_{10} = -\frac{1}{8}\frac{a\psi}{\varpi(\varpi + \omega_L)},$$

$$A_{11} = -\frac{1}{16}\frac{\xi a^3\omega_L}{(\varpi + 2\omega_L)(\varpi + \omega_L)},$$

$$A_{12} = -\frac{1}{16}\frac{\xi a^3\omega_L}{(\varpi - \omega_L)(\varpi - 2\omega_L)},\ \ A_{13} = \frac{1}{2}\frac{2K - a^2}{{\omega_L}^2}$$

4. Numerical validation

In this study, the MMS was used to investigate the steady state response, and Runge-Kutta Method was also utilized for numerical validation. The steady state response is illustrated in Fig. 2 for an excitation frequency $\varpi = 2 \times 10^6\ rad/s$, a magnetic field intensity B_m of 0.15 T, an initial rise V_0 of 0.5 nm, a temperature increment ΔT of 0 ℃, and an initial displacement w_i of 1 nm. Fig. 3 shows the steady state response with the following parameters: $\varpi = 3 \times 10^7\ rad/s$, $B_m = 0.1\ T$, $V_0 = 0.1nm$, $\Delta T = 0$ ℃, and $w_i = 1\ nm$. A solid line represents the approximate analytical solution using the MMS, and markers represent the numerical solution. It is clearfrom Fig. 2 and Fig. 3 the numerical results show excellent agreement with the analytical response utilizing the MMS.

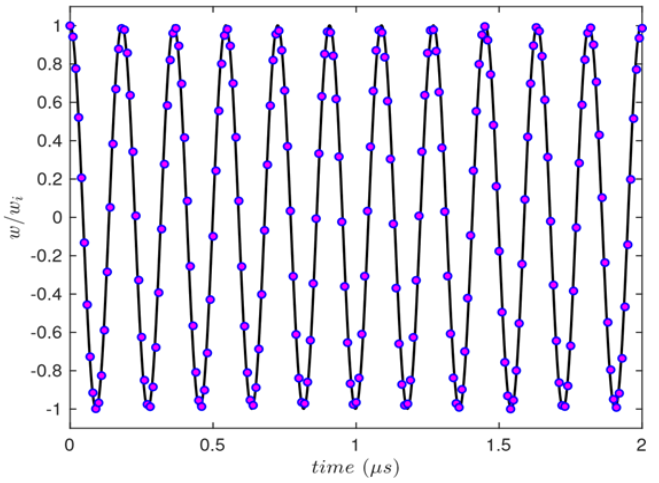

Fig. 2: Steady state response for $\varpi = 2 \times 10^6\ rad/s$, $B_m = 0.15$ T, $V_0 = 0.5$ nm, $\Delta T = 0$ ℃, and $w_i = 1\ nm$. A solid line represents the approximate analytical solution using the MMS, and markers represent the numerical solution.

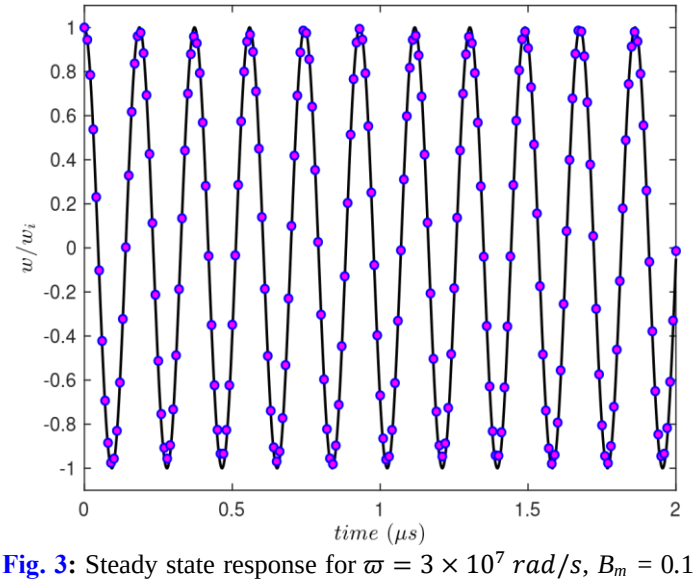

Fig. 3: Steady state response for $\varpi = 3 \times 10^7\ rad/s$, $B_m = 0.1$ T, $V_0 = 0.1$ nm, $\Delta T = 0.5$ ℃, and $w_i = 1\ nm$. A solid line represents the approximate analytical solution using the MMS, and markers represent the numerical solution.

5. Results and discussion

In order to examine the dynamical behavior of an imperfect microbeam under periodic magnetic excitation and thermal loading, we consider a microbeam made of low-carbon steel. The systems physical, geometric, electric, magnetic, and mechanical are outlined in Table 1.

5.1 Dynamic instability

The dynamic instability region is influenced by the initial rise, increased temperature, magnetic field, and amplitude of the vibration. Using the incremental harmonic balance method, dynamic instability boundaries were determined for different initial rise values, as shown in Fig. 4, with small dimensionless amplitude $\|a\| = 1 \times 10^{-9}$and with a temperature increment of $\Delta T = 1$ ℃.

Table 1: Geometric, electric, magnetic, and mechanical properties of the system.

Symbol	Quantity (Unit)	Value
L	Length (m)	4×10^{-6}
h	Thickness (m)	4×10^{-8}
d	Width (m)	2×10^{-7}
E	Young's Modulus (Pa)	194×10^{9}
ρ	Density (kg/m^3)	7930
α	Thermal expansion coefficient ($℃^{-1}$)	11×10^{-6}
α_r	Temperature coefficient of resistivity	6.5×10^{-3}
μ_r	Relative permeability (Hm^{-1})	3×10^{3}
μ_0	Vacuum permeability (Hm^{-1})	1.26×10^{-6}
ϑ_0	Resistivity at room temperature (Ωm)	9.68×10^{-8}
$\bar{h}$	Murnaghan's constant	-2.17×10^{13}

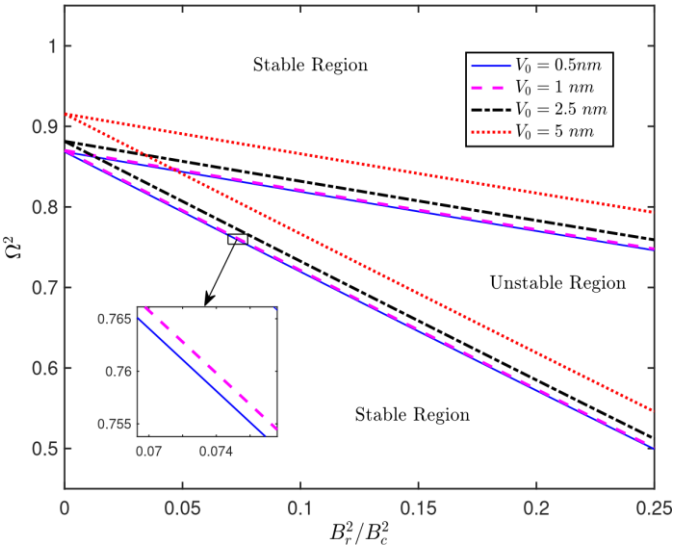

Fig. 4: The influence of the initial rise on the instability region.

The results indicate that as the initial rise value increases, the instability boundary shifts upward. When the initial rise values are less than the amplitude, there is a negligible shift. However, for initial rise values higher than the amplitude, a noticeable shift is observed. This result is reasonable since the initial rise contributes to the stiffness of the system, which in turn increases the excitation frequency of the system.

Considering different temperature increments with $V_0 = 0.5\ nm$, Fig. 5 illustrates the regions of instability. The figure illustrates that as the temperature increment ΔT increases, the instability region shifts downward.

As the temperature increases, the system stiffness reduces. As a result, the instability area shifts downward to lower frequency regions. Additionally, Fig. 6 shows the instability regions for various dimensionless amplitudes $\|a\|$ under the conditions of $V_0 = 1\ nm$ and $\Delta T = 0$ ℃. The observed trend reveals an upward shift in the instability region as the dimensionless amplitude increases.

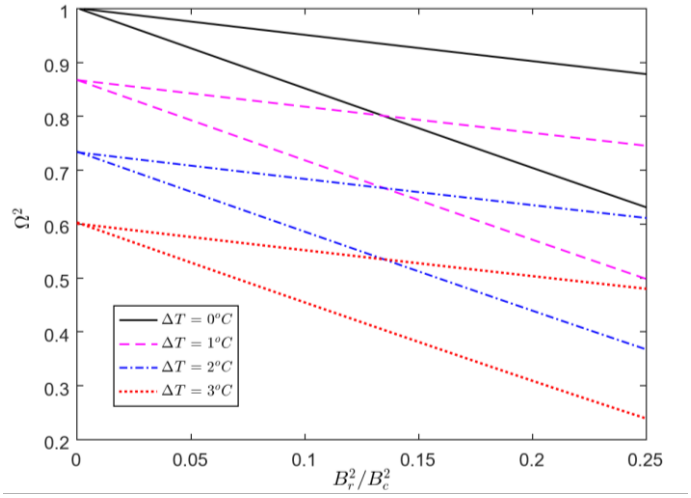

Fig. 5: The impact of thermal load on the instability region.

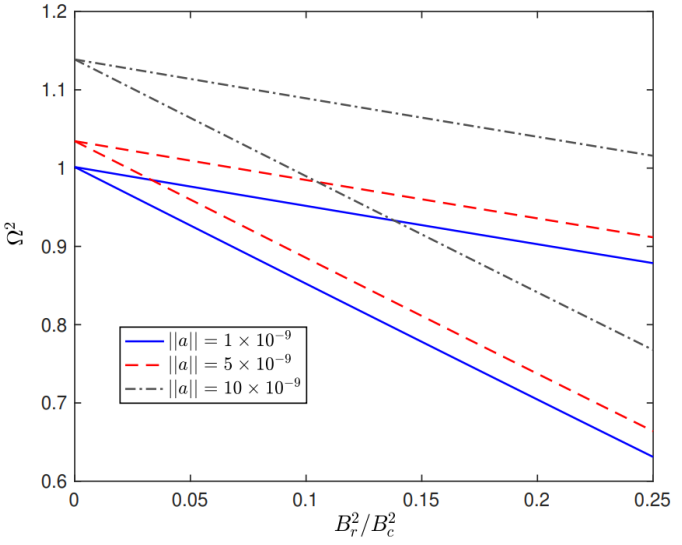

Fig. 6: The influence of the dimensionless amplitude on the instability region.

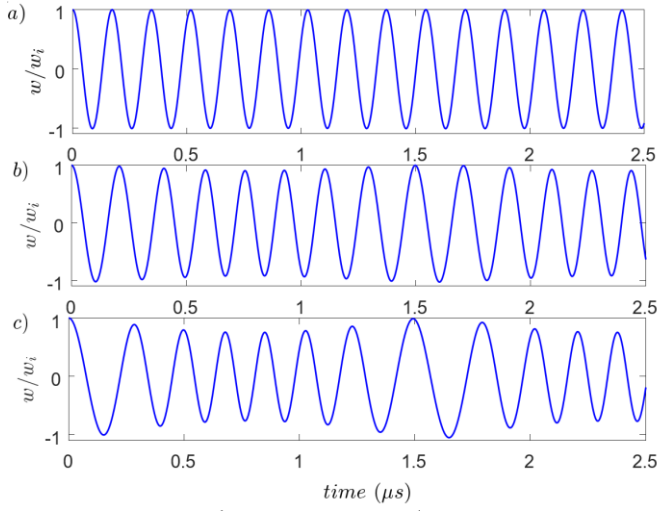

Fig. 7: System's transient response ($V_0 = 5\,nm,\ \Delta T = 0$ ℃, $\varpi = 2 \times 10^6\,rad/s$). Corresponding to various magnetic field intensities: (a) B_m = 0.1 T, (b) B_m = 0.35 T, and (c) B_m = 0.5 T.

5.2 Transient response

The transient vibration of the system under various parameter variations is examined by utilizing the response obtained by using numerical solutions. The dimensionless amplitude versus time at midspan is depicted for various magnetic field intensities ($B_m = 0.1,\ 0.35,\ 0.5$ T) and $\varpi = 2 \times 10^6 rad/s$, while the initial rise and the temperature increment are set to be $V_0 = 5\,nm,\ \Delta T = 0$ ℃, respectively.

These results are respectively shown in Fig. 7 The waveform patterns show that increasing the magnetic field reduces the fundamental frequency. In addition, different temperature increments $\Delta T = 0, 1, 3$ ℃ are applied with no initial rise, while $B_m = 0.25$ T, $\varpi = 8 \times 10^6\ rad/s$ are kept constant. Similarly, an increase in temperature results in a decrease in the fundamental frequency, consistent with Wu *et al.*[15] findings for a microscale beam size. This reduction in the fundamental frequency is caused by increasing the magnetic field amplifies the damping effect. Moreover, the temperature increment affects the damping through the conductivity of the material $\sigma = 1/(\vartheta_0 + \vartheta_0 \alpha_r \Delta T)$. Different temperature increments $\Delta T = 0,\ 1,\ 3$ ℃ are applied while maintaining a constant initial rise $V_0 = 1\,nm$, $B_m = 0.25\,T\ and\ \varpi = 8 \times 10^6\ rad/s$. The outcomes of these variations are shown in Fig. 8, which shows that increasing the temperature increment in presence of initial rise, reduces the peak-to-peak amplitude significantly. The jump in response in Fig. 8 (c) suggests that buckling occurs, leading to a new equilibrium position for the midspan.

It is worth mentioning that all the previous cases were examined in the stable regions. To explore the response across the instability regions, two cases have been considered. In the first case, with no initial rise, the magnetic field intensity B_m and temperature increment ΔT are kept constant at 0.35 T and 0 ℃ while applying different excitation frequencies $\varpi = 2.683 \times 10^7,\ 3 \times 10^7,\ 3.2 \times 10^7\ rad/s$. The results of these variations are depicted in Fig. 9. In the second case, with an initial rise V_0, magnetic field intensity B_m and temperature increment ΔT are maintained constant at $5\,nm, 0.35\,T$ and 1 ℃, respectively, where Fig. 10 illustrates the midspan dimensionless transient response under various natural frequencies $\varpi = 2.924 \times 10^7,\ 3.3 \times 10^7,\ 3.4 \times 10^7\ rad/s$. Furthermore, the presence of the initial rise with thermal load reduces the peak-to-peak amplitude.

In the stability regions near the lower and upper boundaries, stable beating is observed, as shown in Fig. 9 (a), Fig. 9 (c), Fig. 10 (a), and Fig. 10 (c). In contrast, within the instability region, the dimensionless transient response is observed in the form of a pseudo-unstable state, which is a phenomenon related to the resonance of nonlinear Mathieu equations and depends on the initial conditions,[32] as shown in Fig. 9 (b) and Fig. 10 (b). Additionally, the system experiences buckling at an initial rise of $V_0 = 5\,nm$ and a temperature increment of $\Delta T = 1$ ℃, where the midspan oscillates around a new equilibrium position.

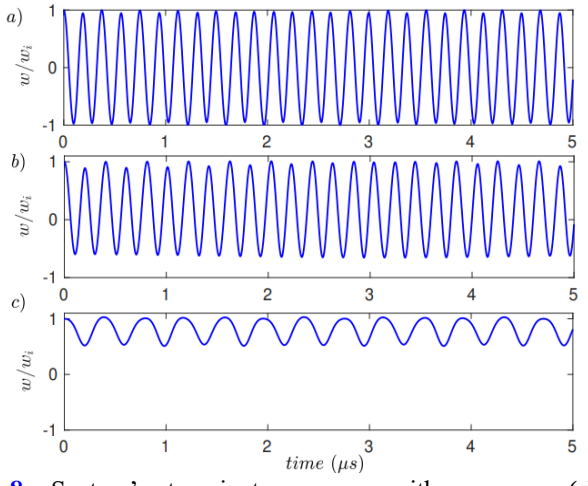

Fig. 8: System's transient response with response ($V_0 = 1\ nm, B_m = 0.25\ T, \varpi = 8 \times 10^6\ rad/s$). Corresponding to various temperatures increments: $(a)\ \Delta T = 0$ ℃, $(b)\ \Delta T = 1$ ℃, $and\ (c)\ \Delta T = 3$ ℃.

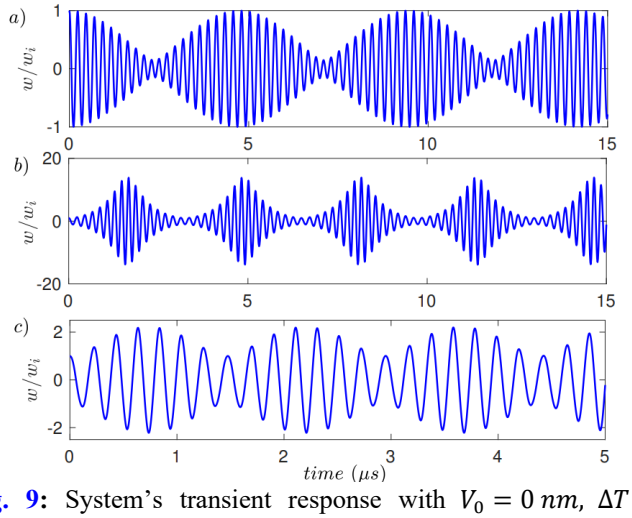

Fig. 9: System's transient response with $V_0 = 0\ nm$, $\Delta T = 0$ ℃ and $B_m = 0.35\ T$. Corresponding to various excitation frequencies: $(a)\ \varpi = 2.683 \times 10^7\ rad/s, (b)\ \varpi = 3 \times 10^7\ rad/s,\ and\ (c)\ \varpi = 3.2 \times 10^7\ rad/s$.

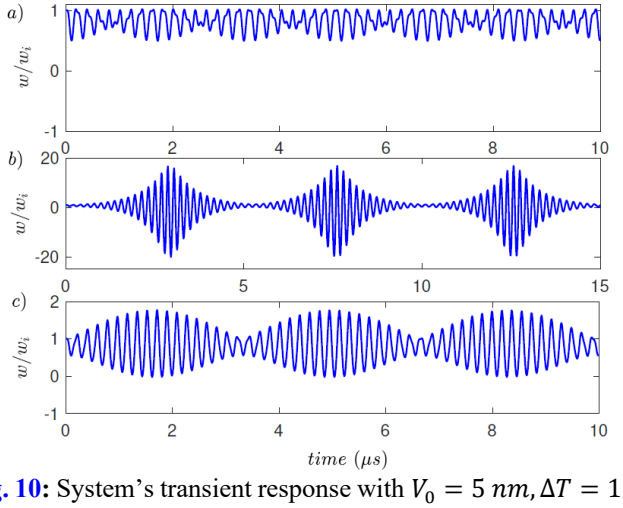

Fig. 10: System's transient response with $V_0 = 5\ nm, \Delta T = 1$ ℃, $and\ B_m = 0.35\ T$. Corresponding to various excitation frequencies: $(a)\ \varpi = 2.924 \times 10^7\ rad/s,\ (b)\ \varpi = 3.3 \times 10^7\ rad/s,\ and\ (c)\ \varpi = 3.4 \times 10^7\ rad/s$.

6. Conclusion

In this study, we investigated the dynamic instability of a magnetoelastic microbeam with an initial rise exposed to a periodic transverse magnetic field and thermal load. The mathematical model has been derived using Galerkin's method and Hamilton's principle. Stability analysis was conducted using the Incremental Harmonic Balance method. The transient responses were obtained by implementing the MMS validated against numerical analysis. It was shown that increasing the initial rise value V_0 shifts the instability region to higher frequencies. Conversely, increasing thermal load moves the instability region to lower frequencies. Moreover, the Instability region has significant sensitivity to the excitation amplitude. A significant shift in instability to a higher frequency range occurs when the vibration's amplitude increases. The transverse magnetic field intensity and temperature increase cause a decrease in fundamental frequency. Finally, the increase in temperature, following an initial rise, results in a substantial decrease in both the peak-to-peak amplitude and the fundamental frequency. The investigation, concentrating on small amplitudes, reveals the resonance phenomenon as a pseudo-unstable condition. Beating phenomena close to the instability boundary were observed.

Conflict of Interest

There is no conflict of interest.

Supporting Information

Not applicable.

References

[1] M. K. Mishra, V. Dubey, P. M. Mishra, I. Khan, MEMS technology: a review, *Journal of Engineering Research and Reports*, 2019, 1-24, doi: 10.9734/jerr/2019/v4i116891.

[2] C. M. Ho, S. Tung, G. B. Lee, Y. C. Tai, F. Jiang, T. Tsao, MEMS - A technology for advancements in aerospace engineering, 35th Aerospace Sciences Meeting and Exhibit, Reno, NV, USA, AIAA, 1997, 545, doi: 10.2514/6.1997-545.

[3] D. R. Sparks, Application of MEMS technology in automotive sensors and actuators, Proceedings of the 1998 International Symposium on Micromechatronics and Human Science, Creation of New Industry, November 25-28, Nagoya, Japan, IEEE, 1998, 9-15, doi: 10.1109/MHS.1998.745744.

[4] S. G. Kim, S. Priya, I. Kanno, Piezoelectric MEMS for energy harvesting, *MRS Bulletin*, 2012, **37**, 1039-1050, doi: 10.1557/mrs.2012.275.

[5] C. Chircov, A. M. Grumezescu, Microelectromechanical systems (MEMS) for biomedical applications, *Micromachines*, 2022, **13**, 164, doi: 10.3390/mi13020164.

[6] S. Park, D. Hah, Pre-shaped buckled-beam actuators: theory and experiments, *Sensors and Actuators A: Physical*, 2008, **148**, 186-192, doi: 10.1016/j.sna.2008.07.009.

[7] P. G Saiz, R. Fernández de Luis, A. Lasheras, M. I. Arriortua, A. C. Lopes, Magnetoelastic resonance sensors: principles, applications, and perspectives, *ACS Sensors*, 2022, **7**, 1248-1268, doi: 10.1021/acssensors.2c00032.
[8] S. R. Green, Y. B. Gianchandani, Microfabricated magnetoelastic sensors and actuators: opportunities and challenges, 2015 IEEE SENSORS, November 1-4, Busan, Korea (South), IEEE, 2015, 1-4, doi: 10.1109/ICSENS.2015.7370368.
[9] F. C. Moon, Y. H. Pao, Magnetoelastic buckling of a thin plate, *Journal of Applied Mechanics*, 1968, **35**, 53-58, doi: 10.1115/1.3601173.
[10] F. C. Moon, Y. H. Pao, Vibration and dynamic instability of a beam-plate in a transverse magnetic field, *Journal of Applied Mechanics*, 1969, **36**, 92-100, doi: 10.1115/1.3564592.
[11] J. Dalrymple, M. Peach and G. Viegelahn, Magnetoelastic buckling: Theory vs. experiment: Paper presents an investigation of the conditions which must be satisfied in an experimental program in order to check theoretical predictions of magnetoelastic buckling fields, *Experimental Mechanics*, 1976, **16**, 26, doi: 10.1007/BF02328918
[12] K. Miya, T. Takagi, Y. Ando, Finite-element analysis of magnetoelastic buckling of ferromagnetic beam plate, *Journal of Applied Mechanics*, 1980, **47**, 377-382, doi: 10.1115/1.3153672.
[13] N. S. Christopherson, M. O. Peach, J. M. Dalrymphle, Magnetostatic deformation experiment: Bending of a thin plate, *Experimental Mechanics*, 1989, **29**, 432-436, doi: 10.1007/BF02323863.
[14] Y. S. Shih, G. Wu, E. J. S. Chen, Transient vibrations of a simply-supported beam with axial loads and transverse magnetic fields, *Mechanics of Structures and Machines*, 1998, **26**, 115-130, doi: 10.1080/08905459808945423.
[15] G. Wu, R. Tsai, Y. Shih, The analysis of dynamic stability and vibration motions of a cantilever beam with axial loads and transverse magnetic fields, *The Journal of the Acoustical Society of America*, 1997, **4**, 40-55.
[16] G. Wu, The analysis of dynamic instability and vibration motions of a pinned beam with transverse magnetic fields and thermal loads, *Journal of Sound and Vibration*, 2005, **284**, 343-360, doi: 10.1016/j.jsv.2004.06.034.
[17] G. Wu, The analysis of dynamic instability on the large amplitude vibrations of a beam with transverse magnetic fields and thermal loads, *Journal of Sound and Vibration*, 2007, **302**, 167-177, doi: 10.1016/j.jsv.2006.11.012.
[18] Q. S. Lu, C. W. S. To, K. L. Huang, Dynamic stability and bifurcation of an alternating load and magnetic field excited magnetoelastic beam, *Journal of Sound and Vibration*, 1995, **181**, 873-891, doi: 10.1006/jsvi.1995.0175.
[19] L. Wang, W. Liu, H. Dai, Dynamics and instability of current-carrying microbeams in a longitudinal magnetic field, *Physica E: Low-Dimensional Systems and Nanostructures*, 2015, **66**, 87-92, doi: 10.1016/j.physe.2014.10.010.
[20] V. Hieu- Dang, Q. Duy-Le, K. Thoa-Nguyen, Nonlinear vibration of microbeams under magnetic field using the modified couple stress theory, *Asian Research Journal of Mathematics*, 2019, **12**, 1-14, doi: 10.9734/arjom/2019/46392.
[21] M. Mahdavi Adeli, R. Mahmoudi and A. Soleimani, Pull-in behaviour of a micro switch actuated by the electrostatic under a uniform longitudinal magnetic field based on nonlocal couple stress theory, *Journal of Computational Applied Mechanics*, 2023, **54**, 577, doi: 10.22059/jcamech.2023.364306.862
[22] D. V. Hieu, N. T. Hoa, L. Q. Duy, N. T. Kim Thoa, Nonlinear vibration of an electrostatically actuated functionally graded microbeam under longitudinal magnetic field, *Journal of Applied and Computational Mechanics*, 2021, **7**, 1537, doi: 10.22055/jacm.2021.35504.2670
[23] I. Esen, Ö. Cevat, M. A. Eltaher, Free vibration of a cracked FG microbeam embedded in an elastic matrix and exposed to magnetic field in a thermal environment, *Composite Structures*, 2021, **261**, 113552, doi: 10.1016/j.compstruct.2021.113552.
[24] H. Hussein, I. Younis Mohammad, Analytical study of the snap-through and bistability of beams with arbitrarily initial shape, *Journal of Mechanisms and Robotics*, 2020, **12**, 1-12, doi:10.1115/1.4045844.
[25] F. Allahkarami, M. Nikkhah-bahrami, M. Saryazdi, Nonlinear forced vibration of FG-CNTs-reinforced curved microbeam based on strain gradient theory considering out-of-plane motion, *Steel and Composite Structures*, 2018, **26**, 673-691, doi: 10.12989/SCS.2018.26.6.673.
[26] E. Arshid, H. Arshid, S. Amir, S. B. Mousavi, Free vibration and buckling analyses of FG porous sandwich curved microbeams in thermal environment under magnetic field based on modified couple stress theory, *Archives of Civil and Mechanical Engineering*, 2021, **21**, 6, doi: 10.1007/s43452-020-00150-x.
[27] S. Lau, Y. Cheung, S. Wu, A variable parameter incrementation method for dynamic instability of linear and nonlinear elastic systems, *Journal of Applied Mechanics*, 1982, **49**, 849-853, doi: 10.1115/1.3162626.
[28] T. Je¸kot, Nonlinear problems of thermal postbuckling of a beam, *Journal of Thermal Stresses*, 1996, **19**, 359-367, doi: 10.1080/01495739608946180.
[29] W. Flügge, Handbook of engineering mechanics, *Journal of Applied Mechanics*, 1963, **30**, 159, doi: 10.1115/1.3630093.
[30] S. L. Lau, S. W. Yuen, Solution diagram of non-linear dynamic systems by the IHB method, *Journal of Sound and Vibration*, 1993, **167**, 303-316, doi: 10.1006/jsvi.1993.1337.
[31] A. Nayfeh, B. Balachandran, Applied nonlinear dynamics: analytical, computational, and experimental methods, New Jersey, John Wiley & Sons, 2022, 700, ISBN: 978-3-527-61755-5.
[32] H. Kidachi and H. Onogi, Note on the stability of the nonlinear Mathieu equation, *Progress of theoretical physics*, 1997, **98**, 755-773, doi: 10.1143/PTP.98.755.